

A Metal-Cap Wedge Shape Hybrid Plasmonic Waveguide for Nano-Scale Light Confinement and Long Propagation Range

Santosh Kumar

National Institute of Technology Patna

Pintu Kumar

National Institute of Technology Patna

Rakesh Ranjan (✉ rr@nitp.ac.in)

National Institute of Technology Patna <https://orcid.org/0000-0003-0022-0516>

Research Article

Keywords: Surface plasmon polaritons, Photonic integration circuits, Hybrid plasmonic waveguide, Propagation length, Coupling length,

Posted Date: May 4th, 2021

DOI: <https://doi.org/10.21203/rs.3.rs-404063/v1>

License:  This work is licensed under a Creative Commons Attribution 4.0 International License.

[Read Full License](#)

Version of Record: A version of this preprint was published at Plasmonics on July 20th, 2021. See the published version at <https://doi.org/10.1007/s11468-021-01502-w>.

A Metal-Cap Wedge Shape Hybrid Plasmonic Waveguide for Nano-Scale Light Confinement and Long Propagation Range

Santosh Kumar, Pintu Kumar, and Rakesh Ranjan
OFC and Photonics Research Lab,
Department of Electronics and Communication Engineering,
National Institute of Technology Patna, India.
*E-mail: rr@nitp.ac.in

Abstract. A metal-cap wedge shape hybrid plasmonic waveguide (WSHPW) has been investigated, for the nano-scale light confinement and long propagation range, in order to analyze the optical properties, such as propagation length, normalized effective mode area, etc., of the fundamental hybrid mode at the wavelength of 1550 nm. Due to the wedge shape structure of high-index region (AlGaAs), the energy is mostly confined at the top of it, inside the low-index region. This results in significant improvement in the propagation length. The modal analysis has been done, using the finite element method, by varying the width of waveguide, wedge angle, permittivity of high- and low-index regions, and heights of metal, high- and low-index regions. The analysis has been further extended for different metal, such as Silver (Ag), Gold (Au) and Aluminum (Al). From the simulation results, it has been established that the propagation length (L_p) > 490 μm , can be achieved for the fundamental mode propagation. Further, the investigations on coupling length (L_c) between the two parallel WSHPWs have been done, which has been achieved as small as 6.10 μm , for the waveguide separation of 100 nm, and waveguide width of 50 nm.

Keywords: Surface plasmon polaritons. Photonic integration circuits. Hybrid plasmonic waveguide. Propagation length. Coupling length.

I. Introduction

For the development of nano-scale optical devices/applications, the optical waveguide is an essential component for its design and practical implementations. In order to achieve the dense photonic integrated circuits (PICs), the optical power loss and guiding the light beyond the diffraction limit, are the main issues. Broadly, the optical waveguides can be categorized in two groups, i.e., conventional/dielectric, and plasmonic waveguides. The optical power loss in the dielectric waveguides is almost negligible, however, it suffers from the diffraction limit [1-4]. Due to diffraction limit, the electromagnetic wave cannot propagate in the waveguide structure, having dimension < $\frac{\lambda}{2n}$, where, n and λ are refractive index of core region and working wavelength of waveguide, respectively [5-7]. Therefore, it is a major issue in order to realize the miniaturized optical waveguide and devices. Moreover, the issue of diffraction limit can be solved by using the approach of surface plasmon polaritons (SPPs), supported by the plasmonic waveguides (PWs) [8, 9]. This waveguide can provide the subwavelength light confinement; however, it is suffering from the large propagation loss, due the presence of metal [10, 11]. Nevertheless, the issues of large propagation loss and diffraction limit can be resolved by another wave-guiding mechanism, known as hybrid plasmonic waveguide (HPW), which essentially combines the mechanisms of dielectric and plasmonic waveguides [12-16]. Different types of the HPWs have been reported in literature [9, 17-21]. Further, the silicon-on-insulator (SOI) based HPWs and optical devices are suffering from monolithic integration with active optical devices at optical communication wavelengths. Whereas, the materials such as, Polytetrafluoroethylene (PTFE), Aluminum Gallium Arsenide (AlGaAs), etc. are the promising materials, capable for the monolithic integration with active optical devices [17, 18]. In this paper, the properties of fundamental hybrid mode of WSHPW have been investigated using the finite element method (FEM). The different dimensions of WSHPW have been varied, in order to achieve the significant propagation length with suitable normalized effective mode area. Further, the optical performance of the fundamental hybrid mode of WSHPW has been investigated by varying the angle of the wedge shape. Due to SPPs, the light has been confined in the smaller contact area inside the low-index region, i.e., between the top of the high-index region (AlGaAs) and metal (Ag) [12, 21].

This paper is arranged as follow. Section II describes the cross sectional view of the metal-cap WSHPW structure. The modal analysis and simulation results have been presented in section III, which is followed by brief discussions and comparison in section IV. Finally, the work has been concluded in section V.

II. Model Description

The cross-sectional view of WSHPW has been illustrated in Fig. 1, where, the metal is placed at top of the wedge shape ridge waveguide structure. The low-index region is separated by metal region and wedge shape high-index region. The materials, AlGaAs and PTFE have been used as high- and low-index regions, respectively. The values of relative permittivity of AlGaAs, and PTFE are, respectively, 12, and 1.7 [18, 27]. The material, AlGaAs has large nonlinear coefficients and negligible nonlinear absorption at the wavelength of 1550 nm. It is also beneficial for the design and implementation of the nonlinear optical devices. Further, the value of the permittivity of metal (Ag) can be calculated using the Drude Model [22, 28], which can be defined as,

$$\varepsilon = \varepsilon_{\infty} - \frac{w_p^2}{w^2 + jw\delta} \quad (1)$$

where, ε_{∞} ($= 3.7$), w_p ($= 1.3946 \times 10^{16} \text{ rad/s}$), and δ ($= 2.7438 \times 10^{13} \text{ s}^{-1}$) are dielectric constant at infinite angular frequency, the bulk plasma frequency, and the damping frequency for silver working at the wavelength of 1550 nm, respectively. Hence, the relative permittivity of metal (Ag) can be obtained as, $\varepsilon_r = -129 + 3.3i$ at 1550 nm [9, 12, 28]. The angle of the wedge has been considered as α . The height of gap (i.e., low index region) between high-index and metal regions, and same for the high index region have been considered as h_g and h_t , respectively; whereas, h_{tr} and w are the height of wedge shape high-index region and the width of waveguide.

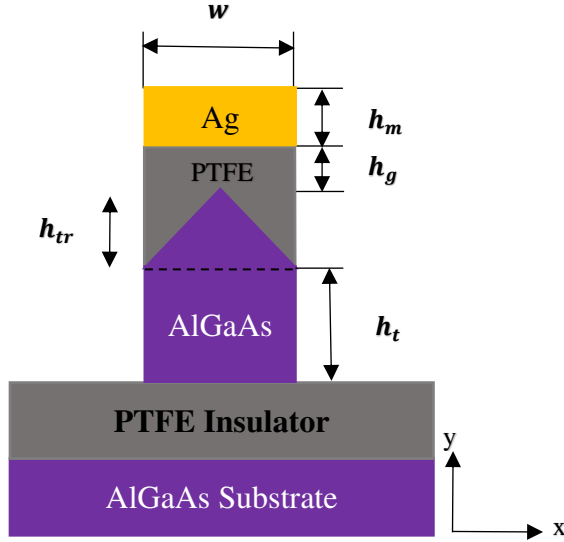


Fig. 1 Cross-sectional view of metal-cap wedge shape hybrid plasmonic waveguide

III. Mode Analysis and Parameter Studies

In the present work, the analysis of properties of fundamental hybrid mode of WSHPW have been investigated using the finite element method (FEM) based 2-D simulator of COMSOL Multiphysics. First, the electric field distributions and its corresponding field profiles, in y-axis direction, have been analyzed and shown respectively in Figs. 2a and 2b, for the waveguide dimensions of $h_{tr} + h_t = 300 \text{ nm}$, $h_m = 100 \text{ nm}$, $h_g = 20 \text{ nm}$, and $w = 200 \text{ nm}$. The efficient design a nano-scale optical waveguides is mainly reliant on two parameters, i.e., propagation length (L_p), and normalized effective area mode (A_{eff}/A_0) of the HPWs. The propagation length of the WSHPW can be defined as the distance over which the amplitude of the energy attenuates to $1/e$ of its input value, and it can be estimated as [23, 24],

$$L_p = \frac{1}{2 \times \text{Im}\{\beta\}} \quad (2)$$

where, β ($= \eta_{eff} \times k_o$) is the propagation constant, k_o ($= \frac{2\pi}{\lambda}$) is the wave vector in vacuum, and η_{eff} is the effective mode index. Furthermore, the effective mode area is an essential parameter for the estimation of the light confinement in the subwavelength region, and it can be estimated as [12, 25],

$$A_{eff} = \frac{1}{\text{Max}\{W(r)\}} \int_{A_\infty} W(r) dA \quad (3)$$

where, $W(r)$ is the energy density and can be expressed as,

$$W(r) = \frac{1}{2} \text{Re} \left\{ \frac{d[\omega \epsilon(r)]}{d\omega} \right\} |E(r)|^2 + \frac{1}{2} \mu_o |H(r)|^2 \quad (4)$$

where, $H(r)$, and $E(r)$ are the magnetic, and electric field intensity, respectively. Further, the ratio, A_{eff}/A_o , can be defined as the normalized effective mode area of the WSHPW. Here, A_o ($= \lambda^2/4$), is the diffraction limited area in free space.

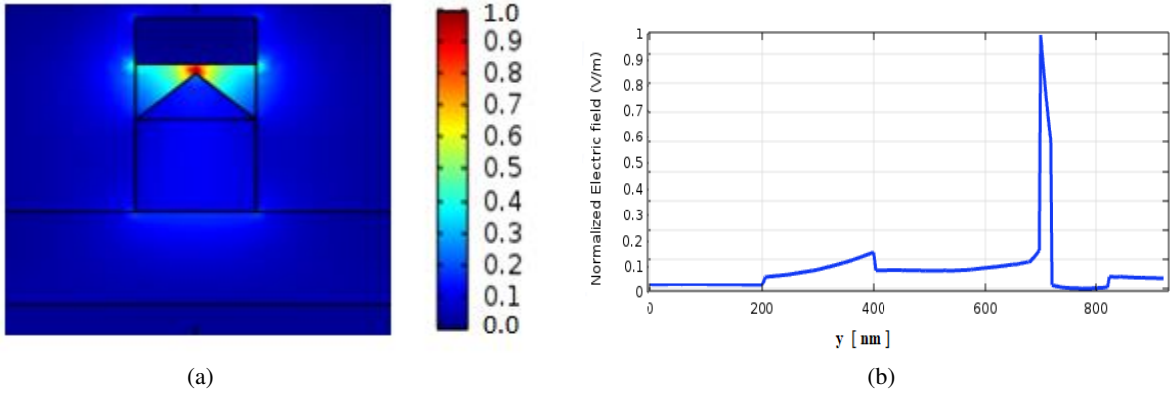


Fig. 2 a Electric field distributions b their corresponding electric field profile, in y-axis direction, for WSHPW with $h_{tr} + h_t = 300 \text{ nm}$, $h_g = 20 \text{ nm}$, $h_m = 100 \text{ nm}$, and $w = 200 \text{ nm}$

A. Effect of Height of Metal on the Propagation Length

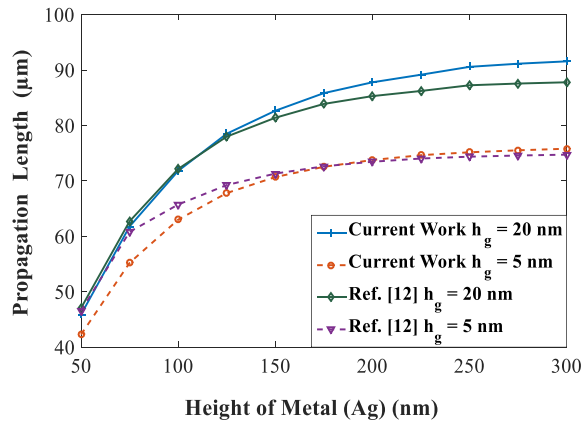


Fig. 3 Comparison of propagation length between the current work and Ref. [12], for $h_{tr} + h_t = 300 \text{ nm}$, $w = 200 \text{ nm}$

In this subsection, the impact of metal height on propagation length has been investigated by varying the value of h_m from 50 nm to 300 nm ; while, w , α , and $h_{tr} + h_t$ have been kept fixed as 200 nm , 60° , and 300 nm , respectively, for two different gaps, i.e., $h_g = 20 \text{ nm}$, and 5 nm . The propagation length of the WSHPW is first increases with the increase in the values of h_m , and then it saturates after $h_m > 175 \text{ nm}$, as depicted in Fig. 3 for both the considered gaps. Further, the obtained results have been compared with the work presented in [12] and from Fig. 3, it is clear that the variations in propagation length is following the similar trend as that of [12]. However, for larger metal heights ($> 150 \text{ nm}$), the improvement in propagation lengths have been observed for $h_g = 20 \text{ nm}$. Moreover, to achieve the

miniaturization of the waveguide dimension and considering both the gaps; the height of metal has been considered as 100 nm for the subsequent analysis.

B. Effect of Width of the WSPW on Fundamental Mode Profile

In this subsection, the impact of waveguide width on the fundamental mode profile in WSPW has been investigated by varying of the waveguide width from 50 nm to 500 nm , for both the considered gaps. Here, the value of h_m , $h_{tr} + h_t$, and α have been fixed respectively as, 100 nm , 300 nm and 45° . From Fig. 4a, it can be observed that the real part of the effective index ($\text{Re}(\eta_{eff})$) is first increases with the increase in waveguide width and after $w > 350\text{ nm}$, it gets saturated. Further, the propagation length of the current waveguide is increasing with the increase in waveguide width, as depicted in Fig. 4b. It is also indicating that the propagation length is larger for the larger gap. This is mainly due to the fact that the impact of conventional plasmonic structure (due to Ag-AlGaAs) is more on the HPW. Moreover, from Fig. 4b, it can be recognized that the obtained propagation length is decently more than that reported in [12]. For example, L_p has been achieved around $\sim 140\ \mu\text{m}$, and $\sim 101\ \mu\text{m}$ at $h_g = 20\text{ nm}$, and 5 nm , respectively, for $w = 500\text{ nm}$, which have been depicted respectively as $\sim 129\ \mu\text{m}$ and $\sim 87\ \mu\text{m}$, in [12]. However, Fig. 4c illustrates the variations in the normalized effective mode area (A_{eff}/A_0) with respect to the waveguide width, which are comparable to that reported in [12].

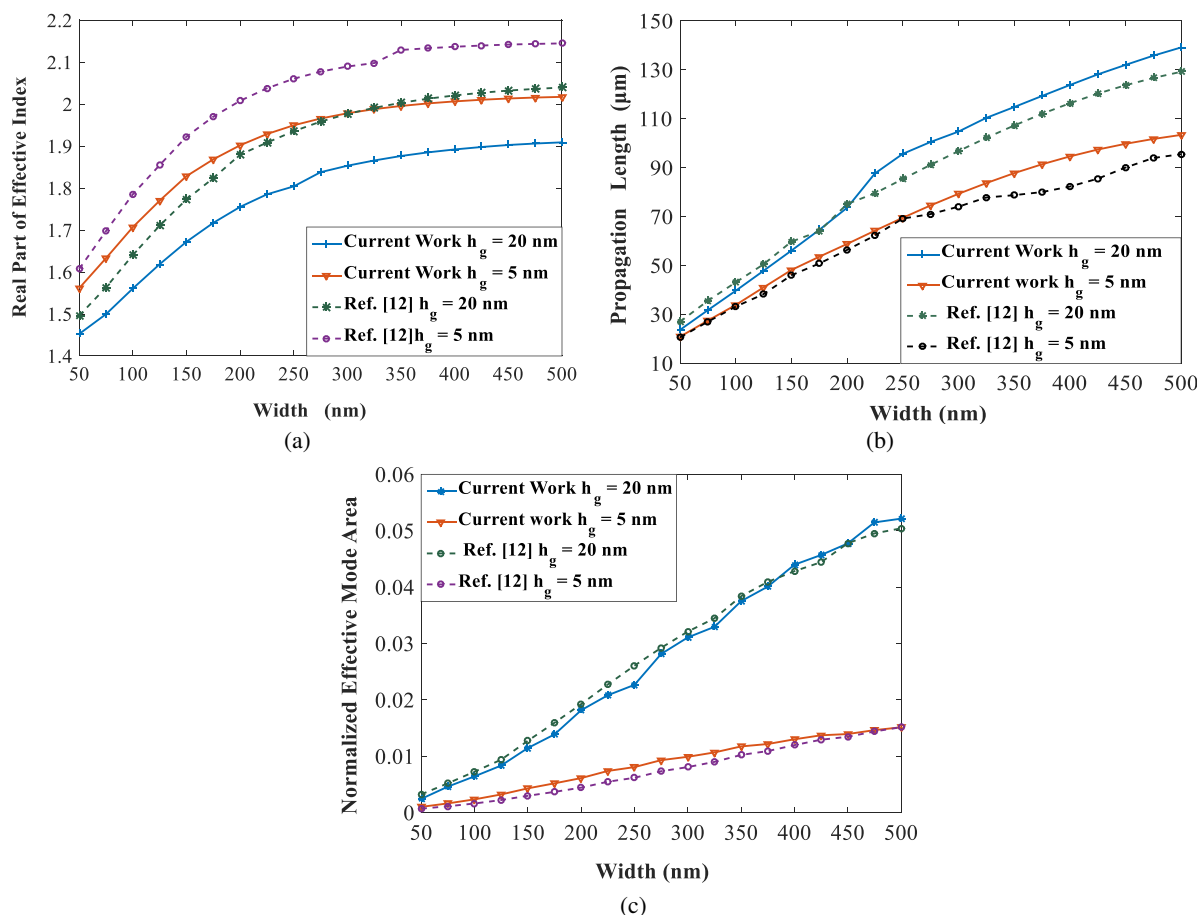


Fig. 4 Comparison of **a** Real part of effective index **b** Propagation length **c** Normalized effective mode area, between the current work and Ref. [12], with respect to waveguide width

Furthermore, Fig. 5 presents the impact of waveguide width on the fundamental mode profile of WSPW, for two different considered gaps and wedge angles (i.e., $\alpha = 45^\circ$, and $\alpha = 20^\circ$). Here, the value of h_m , and $h_{tr} + h_t$ have been fixed at 100 nm , 300 nm , respectively. From the Fig. 5a, it is clear that the propagation length of the current waveguide is increasing with the increase in waveguide width. For example, the values of L_p have been achieved as

$\sim 140 \mu\text{m}$, $\sim 101 \mu\text{m}$, $\sim 150 \mu\text{m}$, and $\sim 95 \mu\text{m}$, respectively at $\alpha = 45^\circ$ and $h_g = 20 \text{ nm}$, $\alpha = 45^\circ$ and $h_g = 5 \text{ nm}$, $\alpha = 20^\circ$ and $h_g = 20 \text{ nm}$, and $\alpha = 20^\circ$ and $h_g = 5 \text{ nm}$, for $w = 500 \text{ nm}$. Further, as depicted in Fig. 5b, A_{eff}/A_0 is increasing with the increase in waveguide width and for a fixed gap value, the lower wedge angle leads to higher normalized effective mode area. This is mainly due to fact that with the decreasing wedge angle, the impact of wedge shape is decreasing, i.e., the light confining area, between the metal and high index region, is increasing [12, 21].

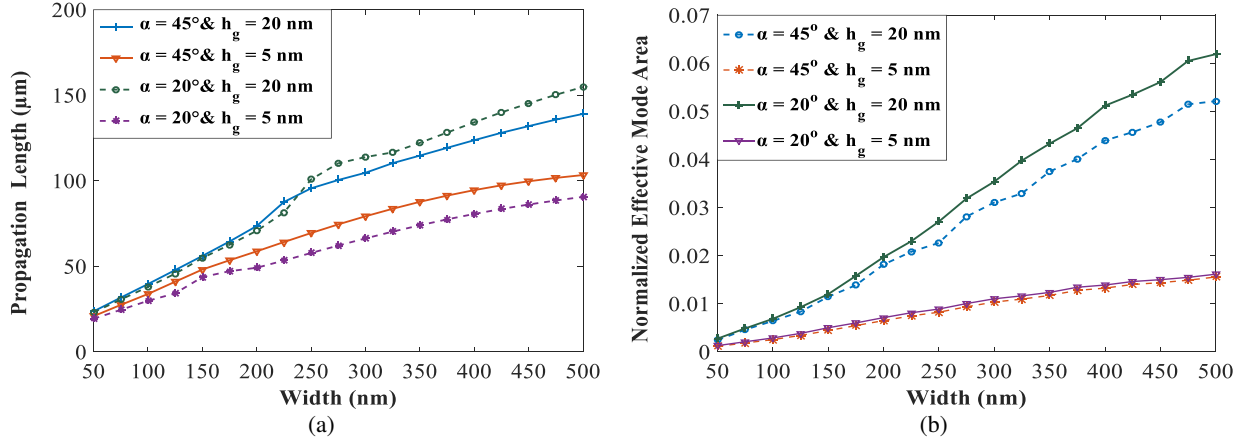


Fig. 5 Comparison of **a** Propagation length **b** Normalized effective mode area, with respect to waveguide width

C. Effect of Wedge Angle on the Propagation Length

In this subsection, the value of w , h_m , and $h_{tr} + h_t$ have been fixed respectively as, 200 nm , 100 nm and 300 nm ; whereas, the wedge angle (α) has been varied from 5° to 60° , for $h_g = 20 \text{ nm}$, and 5 nm , to investigate the impact of wedge angle on the propagation length. As shown in Figs. 6a, and b, the propagation length of the current waveguide is increasing with the increase in wedge angle, respectively for $h_g = 20 \text{ nm}$, and 5 nm . The figure also indicates that for the larger waveguide width, the propagation length is larger. Further, for both the considered values of h_g , the obtained values of propagation length in the current work, are quite better than that reported in [12].

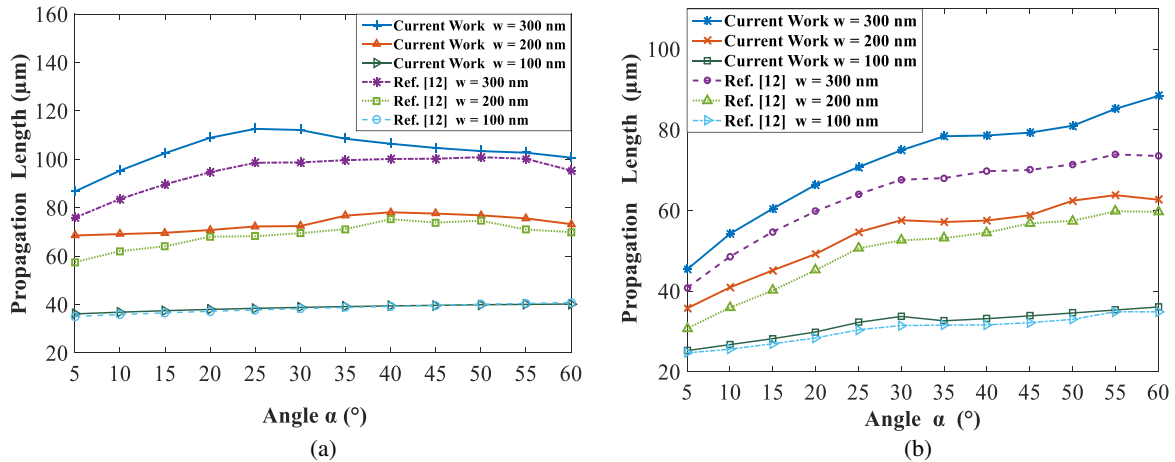


Fig. 6 Variations in Propagation length for **a** $h_g = 20 \text{ nm}$ **b** $h_g = 5 \text{ nm}$, with respect to the wedge angle and its comparison with [12]

D. Effect of Height of High Index (AlGaAs) Region on the Fundamental Mode Profile

Here, the investigations of fundamental mode profile in WSPW have been done by varying of the height of high index region (h_t). Further, the value of h_m , w , and h_{tr} have been fixed respectively at 100 nm , 200 nm , and

100 nm, with $\alpha = 45^\circ$. From the analysis, it is clear that the propagation length of the current waveguide is increasing with the increasing h_t , as depicted in Fig. 7a. The figure also shows that for the larger h_g , the propagation length is larger. This is mainly due to the larger impact of conventional plasmonic nature (due to Ag-AlGaAs) in HPW. From Fig. 7a, it can be observed that the propagation length achieved is quite larger than that reported in [12]. For example, L_p has been achieved around 338 μm at $h_g = 20 \text{ nm}$, and $h_t = 350 \text{ nm}$; whereas, it has been reported as 218 μm at the same waveguide dimension in [12]. However, the obtained normalized effective mode area (A_{eff}/A_0) is a bit more than that reported value in [12], for $h_t > 300 \text{ nm}$, depicted in Fig 7b, which indicates that slightly more energy is confined at the top of the AlGaAs.

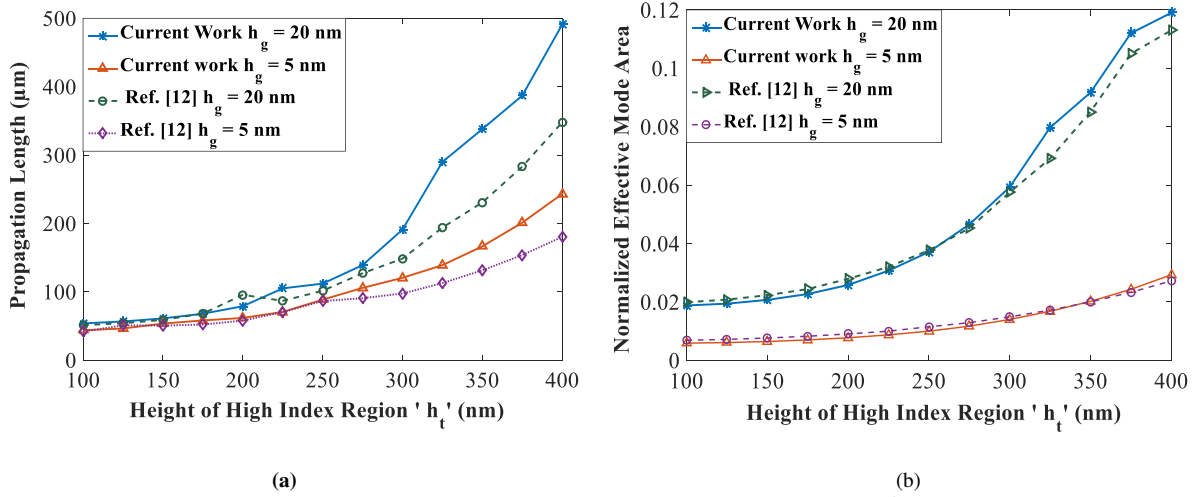


Fig. 7 Variations in **a** Propagation length **b** Normalized Effective mode area with respect to h_t and its comparison with [12]

E. Effect of Different Metal on the Fundamental Mode Profile of the WSHPW

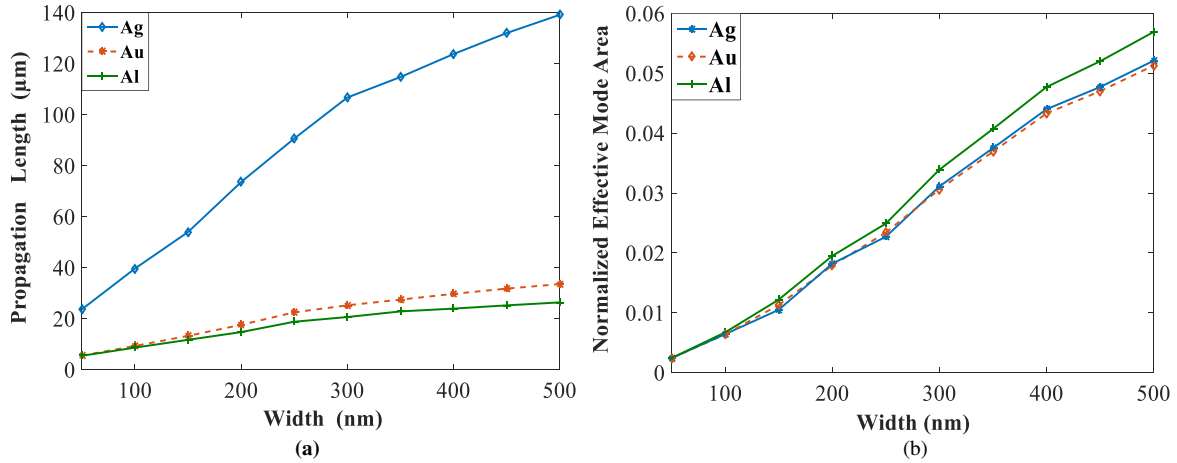


Fig. 8 Comparison of **a** Propagation length **b** Normalized effective mode area for different metals (i.e., Ag, Au, Al)

This subsection presents the investigations of fundamental mode profiles in WSHPW, by varying the waveguide width for different considered metals, such as Silver (Ag), Gold (Au) and Aluminum (Al). For the analysis, the value of $h_m, w, h_{tr} + h_t, h_g$, and α have been considered respectively as, 100 nm, 200 nm, 300 nm, 20 nm, and 45° . The relative permittivity of Au and Al are respectively, $\epsilon_r = -115 + 11.259i$, and $\epsilon_r = -242.68 + 49.433i$, at 1550 nm [26]. From Fig. 8a, it can be observed that propagation length increases with the increasing waveguide width. However, out of the three considered metals, Ag shows the highest propagation length, as compared to other metals, i.e., Au and Al. Further, Fig. 8b illustrates that the normalized effective mode area is increasing with the increase in waveguide width and the metal, Al, provides the highest value of A_{eff}/A_0 , among the three considered metals;

whereas, it have been observed Ag and Au provides the smallest value of A_{eff}/A_0 has been achieved. Hence to designing the nano-scale optical devices Ag is more prefer due to large L_p and smaller A_{eff}/A_0 .

F. Effect of Permittivity of High-Index and Low-Index Regions on the Fundamental Mode Profile of the WSHPW

In this subsection, the impact of change in permittivity of high-index region, on fundamental mode profile has been investigated in terms of propagation length and normalized effective mode area. The permittivity of high index region has been varied from 10 to 14.5 and the values of h_m , $h_{tr} + h_t$, h_g , and α have been fixed at 100 nm, 300 nm, 20 nm, and 45° , respectively. From the analysis, it has been established that propagation length is increasing with the increase in permittivity of high index region, as depicted in Fig. 9a. For the waveguide widths of 100 nm, 200 nm, and 300 nm, the achieved values of the propagation lengths are, $> 40 \mu\text{m}$, $> 95 \mu\text{m}$, and $> 143 \mu\text{m}$, respectively. Figure 9b, shows that the normalized effective mode area increases with the increase in permittivity of high index region. Moreover, it has been observed that for $w = 300 \text{ nm}$, the value of A_{eff}/A_0 is more, as compared to that at $w = 100 \text{ nm}$, and 200 nm.

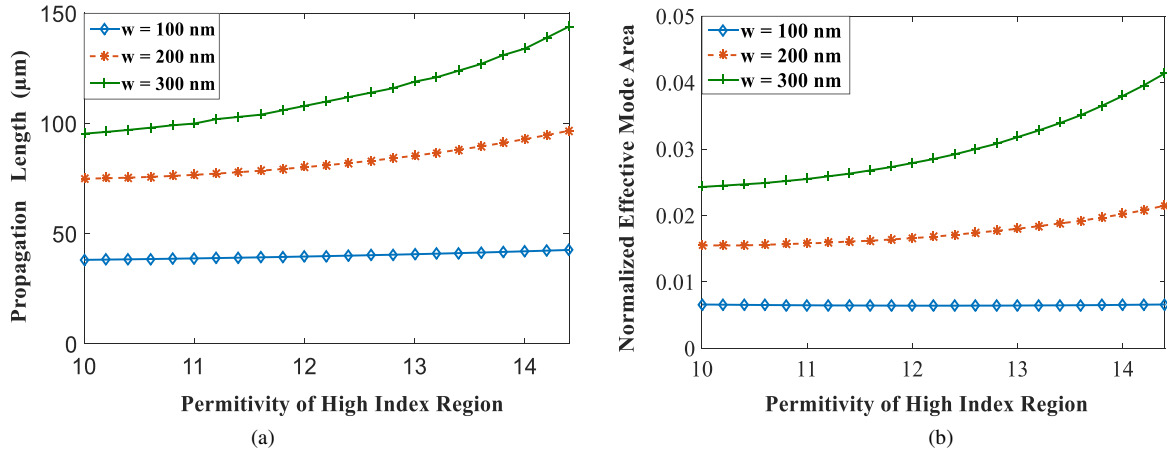


Fig. 9 Comparison of **a** Propagation length **b** Normalized effective mode area with respect to the permittivity of high-index region

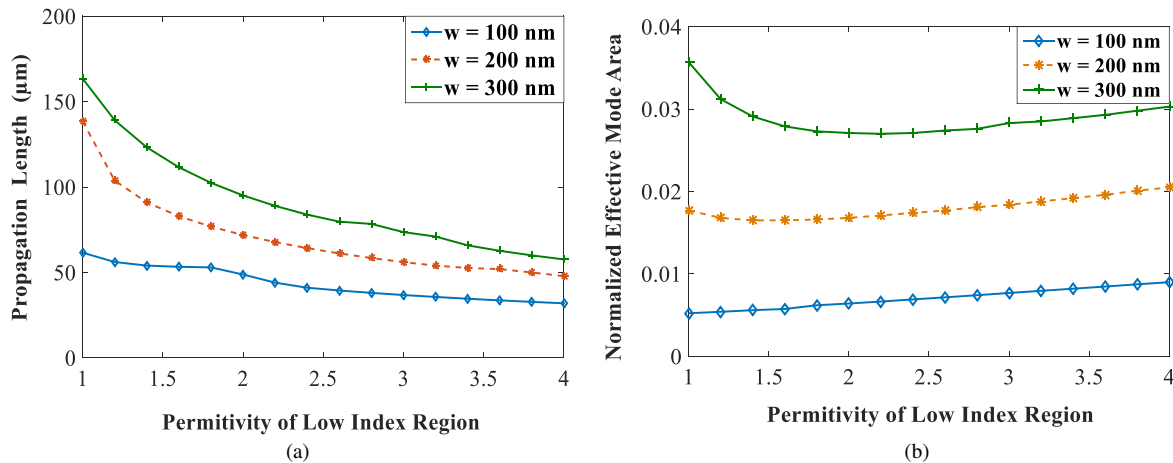


Fig. 10 Comparison of **a** Propagation length **b** Normalized effective mode area with respect to the permittivity of low-index region

The analysis has been further extended by investigating the impact of change in the permittivity of low-index region. Here, the permittivity of low-index region has been varied from 1 to 4 and the value of w , h_m , $h_{tr} + h_t$, h_g , and α have been fixed at 200 nm, 100 nm, 300 nm, 20 nm, and 45° . Figure 10a presents the variations in propagation

length in terms the permittivity of low-index region; where the decrease in propagation length has been observed with the increasing value of low-index permittivity. However, the variations in the normalized effective mode area is usually showing first decreasing nature and then, it increases with the increasing values of low-index permittivity, depicted in Fig 10b.

G. Effect of Separation Distance on the Coupling Length of WSHPW

In the subsection, the coupling phenomena between the two identically parallel WSHPWs have been explored to achieve the compact PICs. Figure 11 shows the cross-sectional view of two parallel WSHPWs, with a separation distance (D) between them. The coupling length (L_c) can be defined as the distance at which the power is completely transferred from one WSHPW to the nearby waveguide and can be expressed as [9],

$$L_c = \frac{\pi}{|\beta_o - \beta_e|} \quad (5)$$

where, β_o and β_e are the propagation constants of the odd and even super-modes of the system of the parallel WSHPWs. The investigations of coupling length have been done by varying the separation distance (D) from 250 nm to 1000 nm with $h_m = 100$ nm. Figure 12a shows the relationship between L_c and D , for different combinations of w and h_g , at $\alpha = 45^\circ$. From the figure, it is clear that L_c increases exponentially with the separation distance and has been achieved as, $> 400 \mu\text{m}$ for $w = 50$ nm and $h_g = 5$ nm. Further, Fig. 12b presents the same relationship between L_c and D at $\alpha = 20^\circ$. In this case also, L_c increases exponentially with D and coupling length, $> 850 \mu\text{m}$, has been achieved with $w = 200$ nm and $h_g = 5$ nm. Moreover, on decreasing D up to 100 nm, the values of L_c have been achieved as $6.10 \mu\text{m}$ ($\alpha = 45^\circ$) and $6.95 \mu\text{m}$ ($\alpha = 20^\circ$), which are quite better than that reported in [9], where it has been reported as, $> 2.8 \mu\text{m}$, at $w = 50$ nm and $h_g = 5$ nm. This essentially helps to realize very compact photonic devices with smaller crosstalk compared to reported in [9].

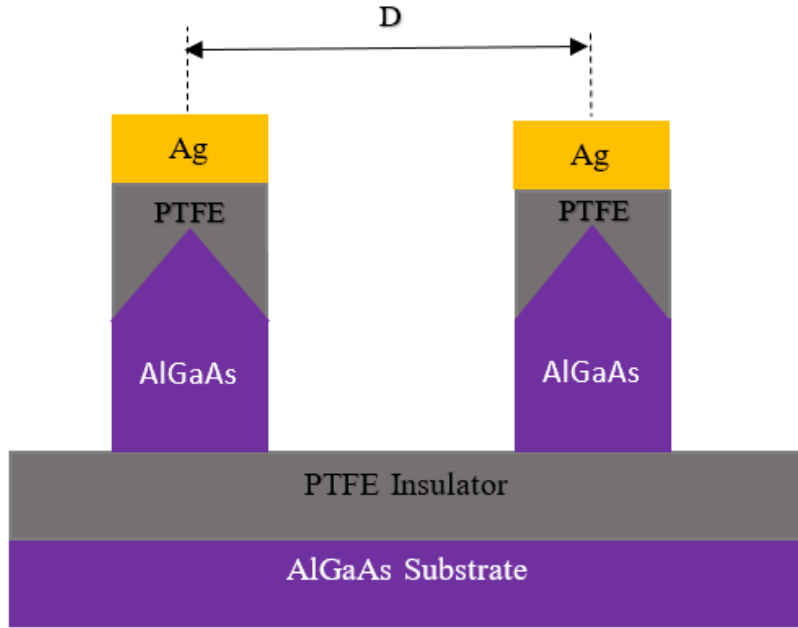


Fig. 11 Cross-sectional view of two identically parallel WSHPWs with a separation distance of D (nm)

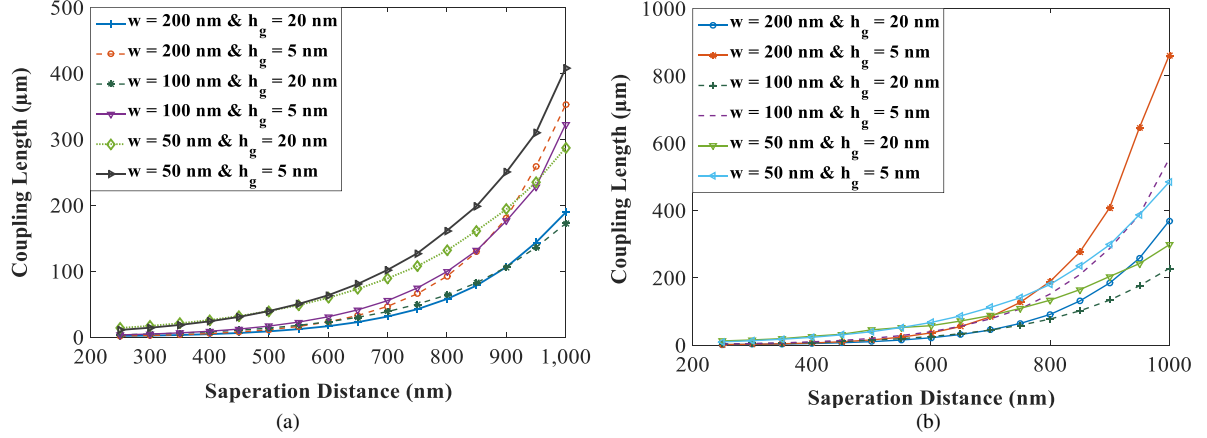


Fig. 12 Variations in Coupling length with respect to the separation distance, for **a** $\alpha = 45^\circ$ **b** $\alpha = 20^\circ$

IV. Discussion

In this paper, the fundamental mode analysis of the guided hybrid modes in metal-cap WSHPW have been done to achieve the subwavelength light confinement along with significantly smaller propagation loss. The investigations have been done over the finite element method based simulation platform, by varying the waveguide width (w), wedge angle (α), and heights of different regions of WSHPW (i.e., h_m , h_t , and h_g), at the wavelength of 1550 nm. The analysis has been further extended by varying the permittivity of high- and low-index regions, and for different metal, such as Ag, Au, and Al. However, for the better performance of the optical waveguides, it should have smaller propagation loss as well as smaller normalized effective mode area. Therefore, achieving the trade-off between propagation length and normalized effective mode area has a vital role for the efficient design of HPWs for some specific applications. From the simulation, the real part of effective index, propagation length, and normalized effective mode area, of the presented WSHPW have been achieved respectively as, 2.24, 188.2 μm , and ~ 0.052 , at $w = 200 \text{ nm}$, $h_m = 100 \text{ nm}$, $h_g = 20 \text{ nm}$, $h_{tr} = 300 \text{ nm}$, $h_t = 100$ and $\alpha = 45^\circ$. This results quite better than that reported in [9, 12]. Moreover, the coupling length of the two identical parallel WSHPWs have been achieved as 6.1 μm , and 6.95 μm , at $D = 100 \text{ nm}$, $w = 50 \text{ nm}$, and $h_g = 5 \text{ nm}$, which are quite better than that reported in [9]. It shows that the small crosstalk between two adjacent waveguides has been achieved for same separation distance, as the higher coupling length leads to lower crosstalk. Table 1 shows the comparison of the current work with the above-mentioned reported work, in term of $\text{Re}(\eta_{eff})$, L_P , A_{eff}/A_0 , and L_C . Further, the coupling length has been analyzed for different waveguide widths, gaps, and wedge angles, which has been achieved as, $> 850 \mu\text{m}$, in the current work. In Fig. 13, the performance of fundamental mode of WSHPW has been investigated, by varying the waveguide width, at $h_m = 200 \text{ nm}$, $h_{tr} + h_t = 300 \text{ nm}$, and $h_g = 20 \text{ nm}$. The propagation loss of WSHPW is increasing for $w < 160 \text{ nm}$, and after, $w > 160$, the propagation loss is reduced. The propagation length of WSHPW has been achieved better than that reported in [12, 19, 21.]. Hence, the WSHPW is beneficial for sub-wavelength light confinement with smaller propagation loss. Moreover, PTFE based metal-cap WSHPW can provide the efficient monolithic integration with active devices, such as photodetector, optical amplifier, optical source, etc.

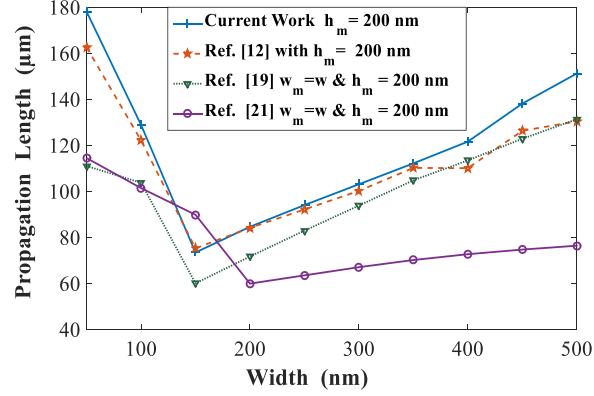


Fig. 13 Comparison of the propagation length with respect to waveguide width, with different hybrid structures [12, 19, 21]

Table 1 Comparison of current work with literature in term of $Re(\eta_{eff})$, L_p , A_{eff}/A_0 , and L_c

Parameters	$Re(\eta_{eff})$	L_p (μm)	(A_{eff}/A_0)	Coupling Length L_c (μm)
Current Work (WSHPW)	2.24	188.2	0.059	6.10 ($\alpha = 45^\circ$) 6.95 ($\alpha = 20^\circ$)
Ref. [12]	2.09	145.3	0.054	--
Ref. [12] (Case I)	2.25	106.3	0.051	--
Ref. [12] (Case II)	2.17	119.8	0.059	--
Ref. [12] (Case III)	2.23	109.2	0.065	--
Ref. [9]	2.38	77.1	0.076	2.38

V. Conclusion

In this paper, the analysis of metal-cap wedge shape hybrid plasmonic waveguide has been presented, in order to achieve the subwavelength light confinement along with the larger propagation length. The fundamental hybrid mode profile has been investigated using the FEM based approach, by varying the different dimensions of the waveguide structure, at the wavelength of 1550 nm. In the current work, the propagation length (L_p) of $> 300 \mu m$ has been achieved, at $h_g = 20 nm$, and $w = 200 nm$ for $h_t > 350 nm$, which is quite better than the recent literatures. However, in order to realize the high photonic integration over the PICs, the crosstalk analysis has established the coupling length (L_c) of the order of $6.10 \mu m$ ($\alpha = 45^\circ$) and $6.95 \mu m$ ($\alpha = 20^\circ$), at the separation distance of $100 nm$, that are quite improved values, at $w = 50 nm$ and $h_g = 5 nm$. This helps to fabricate the very compact photonic devices at smaller crosstalk. Further, the PTFE based metal-cap WSHPW structure can be beneficial to realize its efficient monolithic integration with the active devices, such as optical source, optical amplifier, etc.

Acknowledgments The authors gratefully acknowledge, National Institute of Technology Patna, and Science and Engineering Research Board, Department of Science and Technology, Government of India for providing COMSOL Multiphysics simulation software, used in the current simulation work.

Funding Not Applicable.

Conflict of Interest/ Competing interests The authors declare that they have no conflicts of interest.

Availability of data and materials We reused existing data.

Code availability Not Applicable.

Author Contributions All authors are equally contributed in the manuscript.

References

- [1] Oulton RF, Sorger VJ, Genov DA, Pile DFP, Zhang X (2008) A hybrid plasmonic waveguide for subwavelength confinement and long-range propagation. *Nature Photonics* 2:496-500. <https://doi.org/10.1038/nphoton.2008.131>
- [2] Sorger VJ, Ye Z, Oulton RF, Wang Y, Bartal G, Yin X, Zhang X (2011) Experimental demonstration of low-loss optical wave guiding at deep sub-wavelength scales. *Nature Communications* 2:331. <https://doi.org/10.1038/ncomms1315>
- [3] Eti N, Kuri N (2016) Model analysis of ridge and rib types of silicon waveguides with void compositions. *IEEE Journal of Quantum Electronics* 52: 8400207. <http://doi: 10.1109/JQE.2016.2598082>
- [4] Wang W, Ye H, Wang Q et al (2018) Propagation properties of nanoscale three-dimensional plasmonic waveguide based on hybrid of two fundamental planar optical metal waveguides. *Plasmonics* 13:1615–1621. <https://doi.org/10.1007/s11468-017-0670-6>
- [5] Liu L, Han Z, He S (2005) Novel surface plasmon waveguide for high Integration. *Optics Express* 13:6645. <https://doi.org/10.1364/OPEX.13.006645>
- [6] Pile DFP, Ogawa T, Gramotnev DK, Matsuzaki Y, Vernon KC, Yamaguchi K (2005) Two-dimensionally localized modes of a nanoscale gap plasmon waveguide. *Applied Physics Letters* 87: 261114. <https://doi.org/10.1063/1.2149971>
- [7] Alam MZ, Stewart JA, Mojahedi M (2014) A marriage of convenience: hybridization of surface plasmon and dielectric waveguide modes. *Laser Photonics Reviews* 8:394–408. <https://doi.org/10.1002/lpor.201300168>
- [8] Alam MZ, Aitchison JS, Mojahedi M (2010) Propagation characteristics of hybrid modes supported by metal-low-high index waveguides and bends. *Optics Express* 18:12971-1279. <https://doi.org/10.1364/OE.18.012971>
- [9] Dai D, He S (2009) A silicon-based hybrid plasmonic waveguide with a metal cap for a nano-scale light confinement. *Optics Express* 17:16646–16653. <https://doi.org/10.1364/OE.17.016646>
- [10] Nourmohammadi A, Nikoufard M (2020) Ultra-wideband photonic hybrid plasmonic horn nanoantenna with SOI configuration. *Silicon* 12: 193–198. <https://doi.org/10.1007/s12633-019-00113-9>
- [11] Veronis G, Fan S (2007) Modes of subwavelength plasmonic slot waveguides. *Journal of Lightwave Technology* 25: 2511-2521. <http://doi: 10.1109/JLT.2007.903544>
- [12] Wang J , Guo Y, Huang BH, Gao SP, Xia YS (2019) A silicon-based hybrid plasmonic waveguide for nano-scale optical confinement and long range propagation. *IEEE Transactions on Nanotechnology* 18:437-444. <http://doi: 10.1109/TNANO.2019.2911333>.
- [13] Xiao J et al (2016) A CMOS-compatible hybrid plasmonic slot waveguide with enhanced field confinement. *IEEE Electron Device Letters* 37: 456-458. <http://doi:10.1109/LED.2016.2531990>
- [14] Dizaj LH, Abbasian K, Nurmohammadi, T (2020) A three-core hybrid plasmonic polarization splitter designing based on the hybrid plasmonic waveguide for utilizing in optical integrated circuits. *Plasmonics* 15: 2213–2221. <https://doi.org/10.1007/s11468-020-01249-w>
- [15] Krasavin AV, Zayats AV (2010) Silicon-based plasmonic waveguides. *Optics Express* 18:11791-11799. <https://doi.org/10.1364/OE.18.011791>
- [16] Chen L, Shakya J, Lipson M (2006) Sub wavelength confinement in an integrated metal slot waveguide on silicon. *Optics Letters* 31:2133–2135. <https://doi.org/10.1364/OL.31.002133>
- [17] Nikoufard M, Alamouti MK, and Pourgholi S (2017) Multimode interference power-splitter using inp-based deeply etched hybrid plasmonic waveguide. *IEEE Transactions on Nanotechnology* 16:477-483. <http://doi: 10.1109/TNANO.2017.2688397>
- [18] Kumar P, Singh DK, Ranjan R (2020) Optical performance of hybrid dielectric loaded plasmonic waveguide using PTFE for nano-scale light confinement. *Optoelectronics Letters* 16:284–289. <https://doi.org/10.1007/s11801-020-9119-9>
- [19] Bian Y, Gong Q (2014) Bow-tie hybrid plasmonic waveguides. *Journal of Lightwave Technology* 32:4504-4509. <http://doi: 10.1109/JLT.2014.2359916>.
- [20] Sharma P, Kumar VD (2016) Investigation of multilayer planer hybrid Plasmonic waveguide and bends. *IET Electronics Letters* 52:732-734. <https://doi.org/10.1049/el.2015.3827>
- [21] Lu Q, Zou C ,Chen D , Wu G (2014) Extreme light confinement and low loss in traingular hybrid plasmonic waveguide. *Optics Communications* 319:141-146. <https://doi.org/10.1016/j.optcom.2013.12.072>
- [22] Kumar P, Singh DK, Ranjan R (2018) Mode analysis of hybrid metal-insulator-metal multilayer plasmonic waveguide. *Conference on Information and Communication Technology (CICT), Jabalpur, India* 1-4. <http://doi: 10.1109/INFOCOMTECH.2018.8722355>.
- [23] Aldawsari S, Wei L, Liu W (2017) A comprehensive theoretical study of the guided modes in a five-layer hybrid-metal/dielectric/metal waveguide. *Journal of Lightwave Technology* 35: 2243-2251. <http://doi: 10.1109/JLT.2016.2643507>
- [24] Bian Y, Gong Q (2013) Optical performance of one-dimensional hybrid metal-insulator-metal structures at telecom wavelength. *Optics Communications* 308:30-35. <https://doi: 10.1016/j.optcom.2013.06.034>
- [25] Zhang Y, Zhang Z, (2017) Ultra-subwavelength and low loss in v-shaped hybrid plasmonic waveguide. *Plasmonics* 12,:59–63. <https://doi.org/10.1007/s11468-016-0228-z>
- [26] Refractive Index Database. Available at: <http://refractiveindex.info>.
- [27] Sharma P, and Kumar VD (2016) Investigation of multilayer planar hybrid plasmonic waveguide and bends. *Electronic Letters* 52:732-734. <https://doi.org/10.1049/el.2015.3827>
- [28] Kumar P, Singh DK, Ranjan R (2019) Optical performance of hybrid metal-insulator-metal plasmonic waveguide for low-loss and efficieint photonic integration. *Microwave and Optical Technology Letters* 1-9. <http://doi.org/10.1002/mop.32241>

Figures

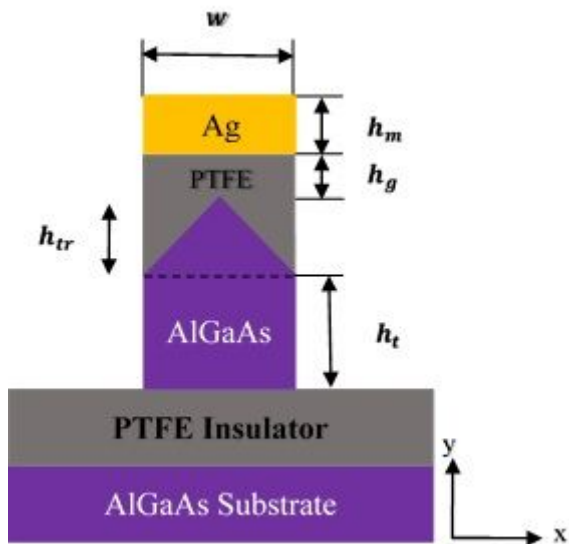


Figure 1

Cross-sectional view of metal-cap wedge shape hybrid plasmonic waveguide

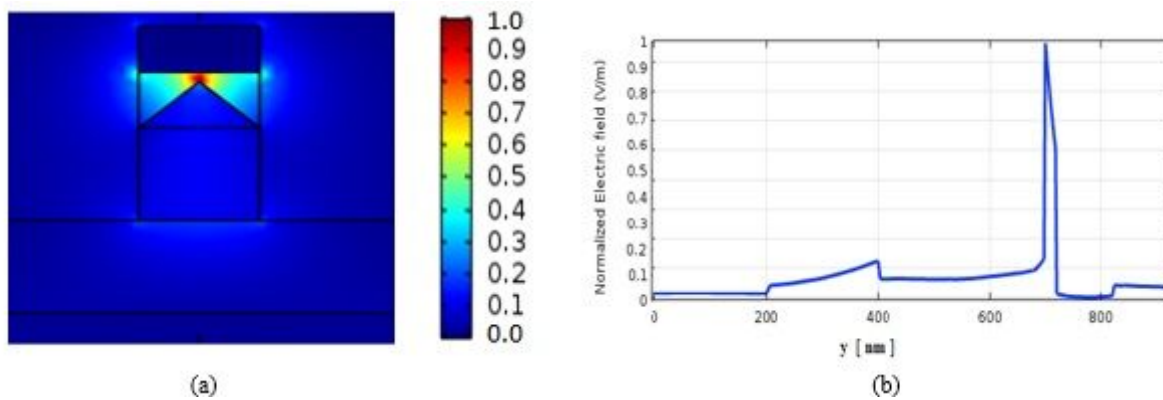


Figure 2

Electric field distributions b their corresponding electric field profile, in y-axis direction, for WSHPW with $h_{tr}+h_t=300$ nm, $h_g=20$ nm, $h_m=100$ nm, and $w=200$ nm

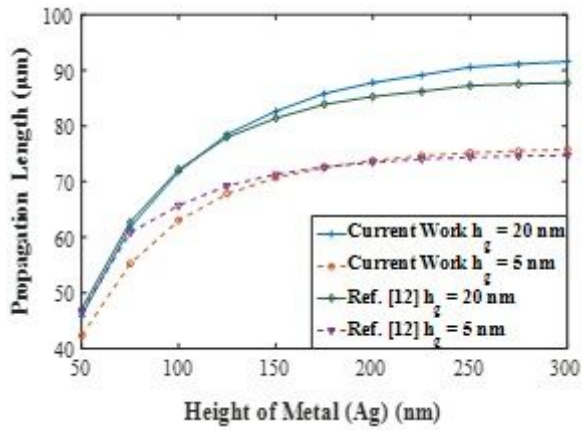


Figure 3

Comparison of propagation length between the current work and Ref. [12], for $h_{tr}+h_t=300$ nm, $w = 200$ nm

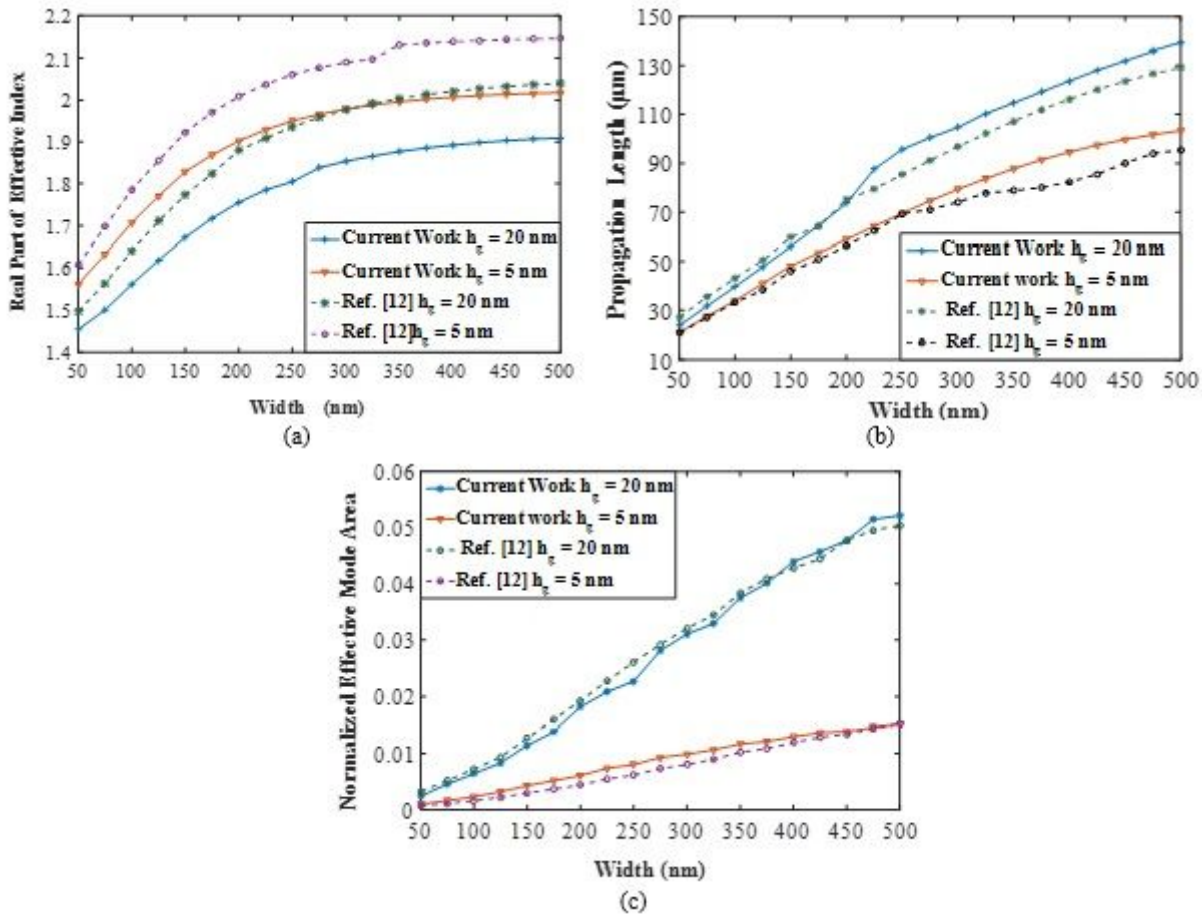


Figure 4

Comparison of a Real part of effective index b Propagation length c Normalized effective mode area, between the current work and Ref. [12], with respect to waveguide width

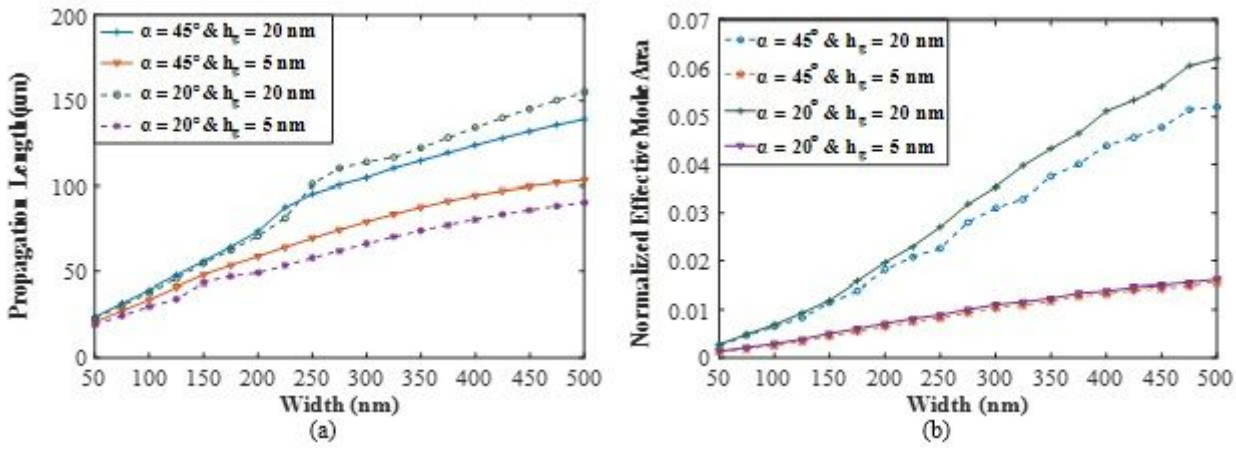


Figure 5

Comparison of a Propagation length b Normalized effective mode area, with respect to waveguide width

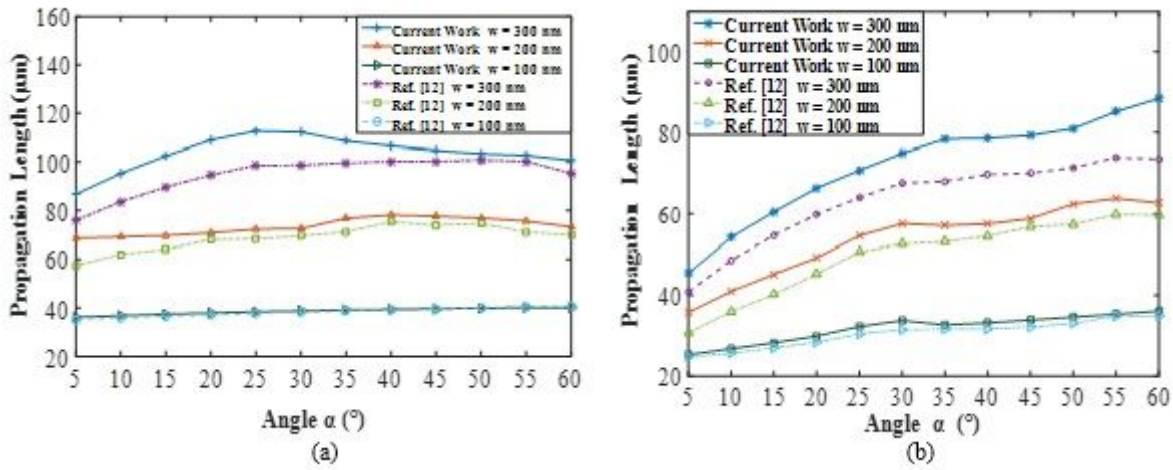


Figure 6

Variations in Propagation length for a $h_g = 20$ nm b $h_g = 5$ nm, with respect to the wedge angle and its comparison with [12]

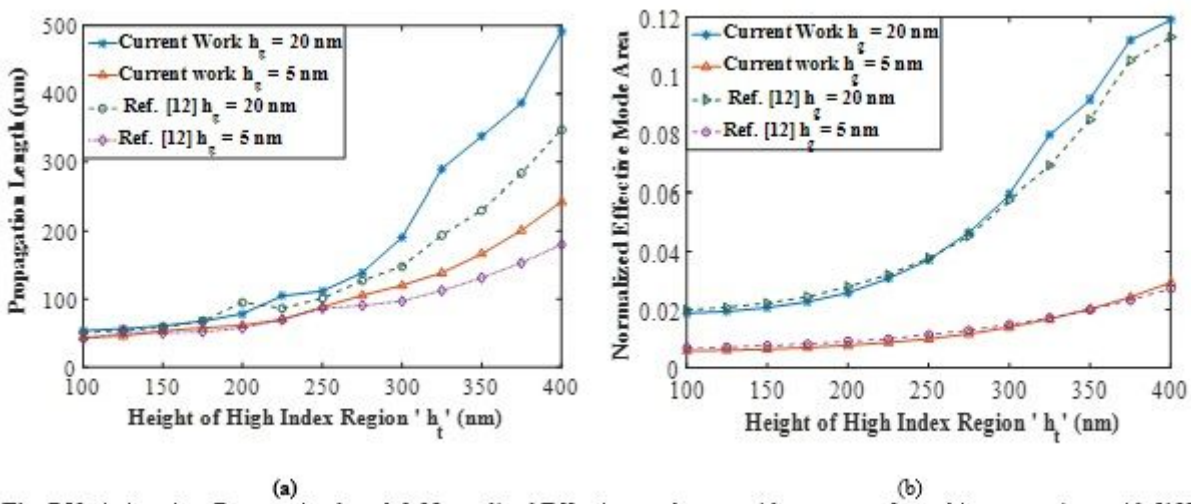


Figure 7

Variations in a Propagation length b Normalized Effective mode area with respect to ht and its comparison with [12]

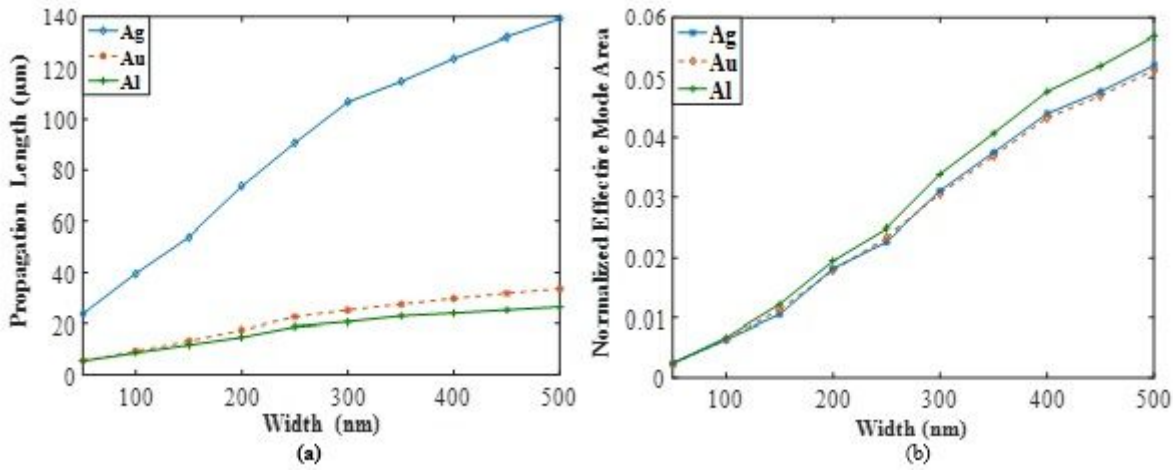


Figure 8

Comparison of a Propagation length b Normalized effective mode area for different metals (i.e., Ag, Au, Al)

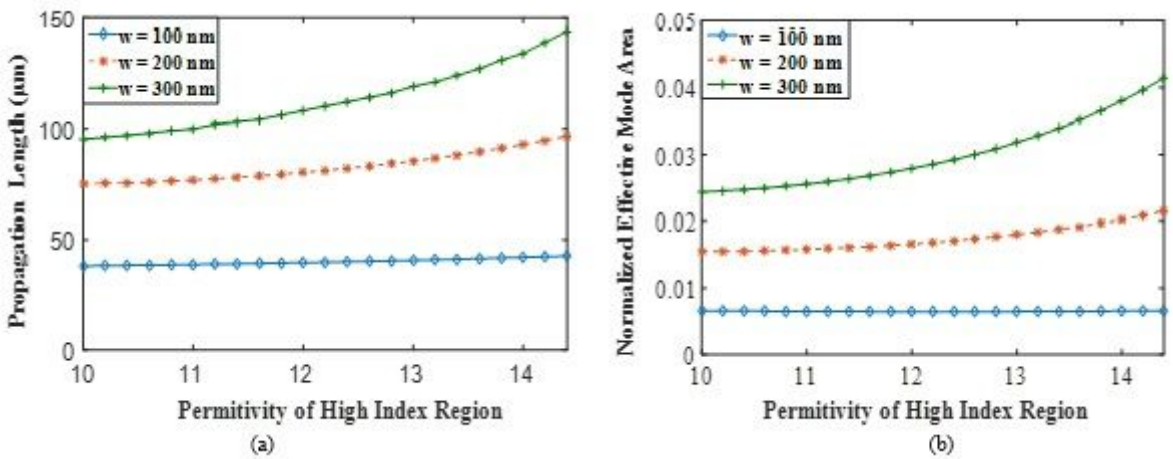


Figure 9

Comparison of a Propagation length b Normalized effective mode area with respect to the permittivity of high-index region

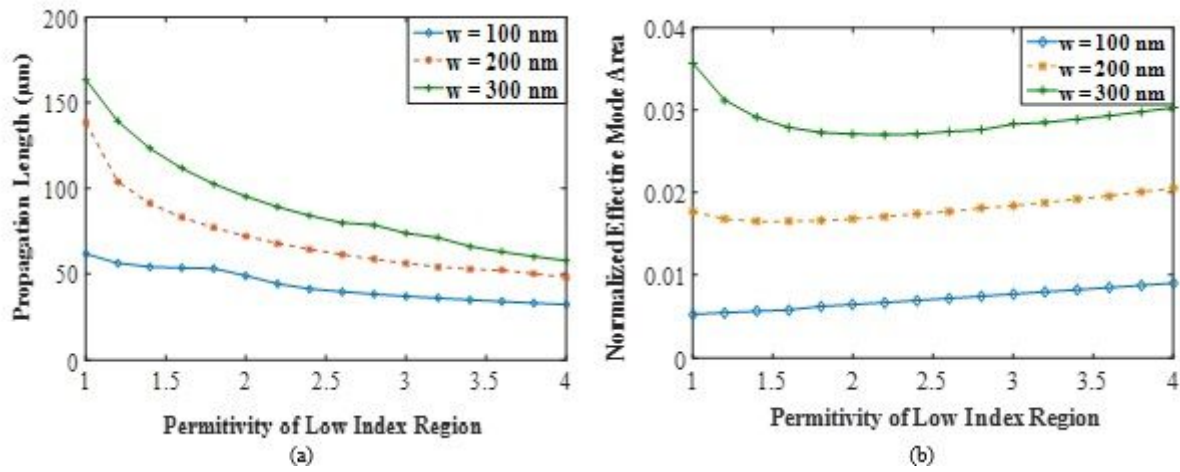


Figure 10

Comparison of a Propagation length b Normalized effective mode area with respect to the permittivity of low-index region

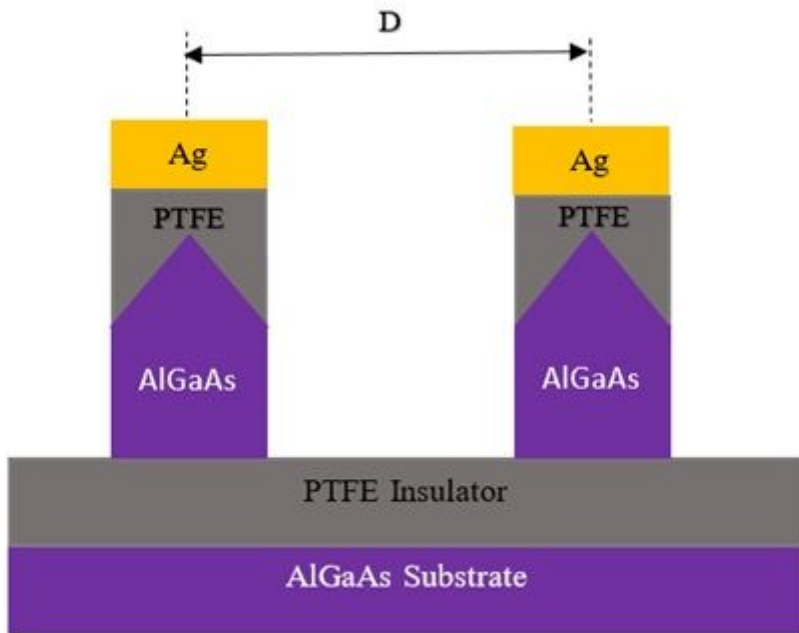


Figure 11

Cross-sectional view of two identically parallel WSHPWs with a separation distance of D (nm)

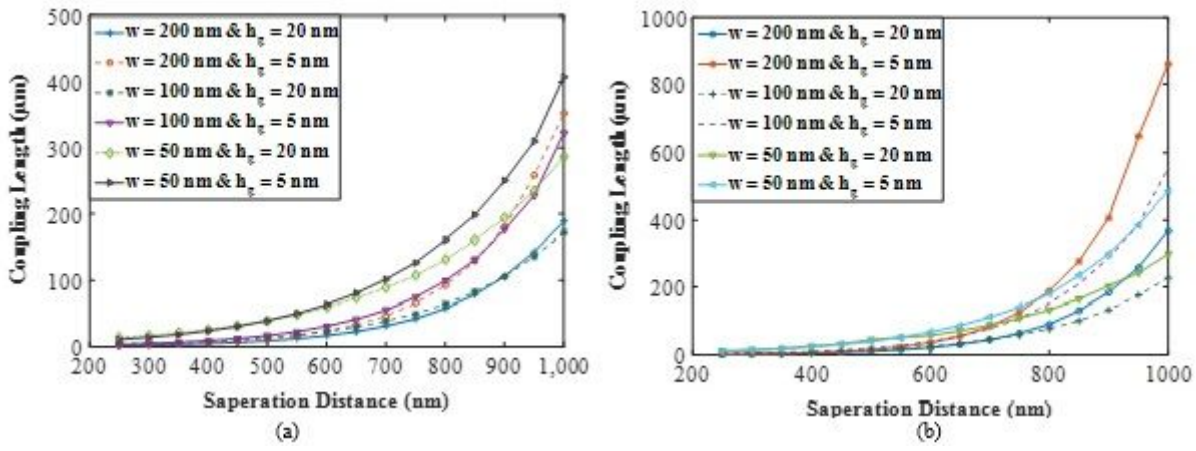


Figure 12

Variations in Coupling length with respect to the separation distance, for a $\alpha=45^\circ$ b $\alpha=20^\circ$

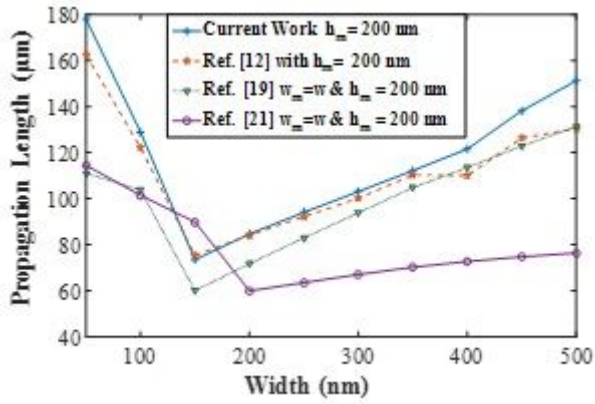


Figure 13

Comparison of the propagation length with respect to waveguide width, with different hybrid structures [12, 19, 21]